Steady-entangled-state generation via the cross-Kerr effect in a ferrimagnetic crystal

Zhi-Bo Yang, Wei-Jiang Wu, Jie Li, Yi-Pu Wang,* and J. Q. You†
Interdisciplinary Center of Quantum Information, State Key Laboratory of Modern Optical Instrumentation, and Zhejiang Province Key Laboratory of Quantum Technology and Device, Department of Physics, Zhejiang University, Hangzhou 310027, China

(Received 26 March 2022; accepted 28 June 2022; published 14 July 2022)

For solid-state spin systems, the collective spin motion in a single crystal embodies multiple magnetostatic modes. Recently, it was found that the cross-Kerr interaction between the higher-order magnetostatic mode and the Kittel mode introduces a new operable degree of freedom. In this work we propose a scheme to entangle two magnon modes via the cross-Kerr nonlinearity when the bias field is inhomogeneous and the system is driven. Quantum entanglement persists at the steady state, as demonstrated by numerical results using experimentally feasible parameters. Furthermore, we also demonstrate that entangled states can survive better in the system where self-Kerr and cross-Kerr nonlinearities coexist. Our work provides insights and guidance for designing experiments to observe entanglement between different degrees of freedom within a single ferrimagnetic crystal. Additionally, it may stimulate potential applications in quantum information processing using spintronic devices.

DOI: 10.1103/PhysRevA.106.012419

I. INTRODUCTION

Manipulation of the light-matter interaction has been a long-standing and intriguing topic owing to its important role in quantum information science. In recent years, cavity magnonics has gradually demonstrated its unique advantages when achieving magnon-based hybrid quantum systems [1–11]. Among the ferrimagnetic materials and microwave ferrites, yttrium iron garnet (YIG) has a high spin density ($\sim 4.22 \times 10^{27}$ m^{-3}) and a low dissipation rate ($\sim$1 MHz). Strong coupling between magnons (quanta of collective spin excitations) in the YIG sphere and cavity photons can be realized, resulting in cavity polaritons [2–6]. Moreover, magnons can also interact with visible or near-infrared light waves (via magneto-optical effect [12–16]), superconducting qubits (indirectly [17–19]), and mechanical deformation modes (directly [20–23]) to form various hybrid systems. Experimental and theoretical studies based on cavity magnonics reveal a variety of phenomena, including magnon dark modes [24], the magnon Kerr effect [25,26], non-Hermitian physics [27–32], magnon-induced transparency [33], and nonclassical states [21–23,34–41].

Entanglement, as a resource for quantum technologies, plays an essential role in quantum computing [42–45], quantum metrology [46,47], and quantum teleportation [48]. In addition, it has expanded our understanding of many physical phenomena, such as superradiance [49], superconductivity [50], and disordered systems [51]. The mechanism by which continuous-variable (CV) entanglement is generated is based on the squeezing-type interactions within the system [52]. In most systems, this type of interaction is induced by nonlinearities such as radiation pressure interactions in optomechanical systems [53,54], magnetostrictive interactions in cavity magnomechanical systems [21,23], the self-nonlinear Kerr effect in cavity magnonic systems [34,40], and other systems that include parametric amplifiers [22,37,39,55]. Also, it exists intrinsically in some particular systems (for instance, the antiferromagnetic system [35,56]). The nonlinearity is typically weak (for example, the magnon self-Kerr coefficient has a magnitude of $\sim$0.1 nHz [57]), but they can be enhanced by driving the associated spin-wave modes with a drive field.

Cross-Kerr interactions, as a type of nonlinear interaction between fields and waves, have been observed in a variety of systems, including superconducting circuits [58–60], atoms [61–63], and ions [64], among others. Recently, the cross-Kerr interaction between the higher-order magnetostatic (HMS) mode and the spin uniform precession mode (referred to as the Kittel mode [65]) in cavity magnonics was experimentally observed [66]. When only one mode is driven, the two spin-wave modes simultaneously undergo nonlinear frequency shift, proving that self- and cross-Kerr effects are simultaneously excited. This nonlinearity enables the formation of entanglement in this system. We anticipate that investigating entanglement properties in such a system is critical for understanding how internal degrees of freedom of the ferrimagnetic crystal are correlated and the effects of different nonlinearities on the entanglement. In light of the importance of producing high-quality entangled photons in quantum computation [67–69], entangled states of magnons may also play a key role in other quantum technologies due to the advantages of controllability, integrability, and reliability in solid-state spin ensembles. In this article we explore the entanglement between two spin-wave modes inside a single ferrimagnetic crystal based on the cross-Kerr effect.

The article is organized as follows. In Sec. II we introduce the fundamental model and derive the effective Hamiltonian. In Sec. III the dissipative equations and the covariance matrix of our proposal are given to quantify the bipartite and tripartite entanglements. In Sec. IV we discuss the cross-Kerr induced

*yipuwang@zju.edu.cn
†jqyou@zju.edu.cn

entanglement with the optimized effective interaction between the three modes. The condition for optimizing the tripartite entanglement is found and confirmed by the parametric transformation process with four-wave mixing. In Sec. V we consider the case where two self-Kerr effects and the cross-Kerr effect coexist. We find that the tripartite entanglement can be enhanced, resulting from the emergence of a new nonlinearity-induced parametric interaction and the enhanced coupling between modes. The numerical results indicate that all entanglements are robust against the temperature changes in the environment. Entanglement detection and application are given in Sec. VI. We summarize our work in Sec. VII.

II. MODEL HAMILTONIAN

We consider a cavity magnonic system consisting of the cavity mode, Kittel mode, and HMS mode, as shown in Fig. 1(a). The spin-wave mode interacts with the cavity photon mode via a magnetic dipole-dipole interaction, while the HMS mode couples to the Kittel mode via mode overlap [66,70,71]. The Hamiltonian of the whole system reads

$$H = H_a + H_b + H_c + H_{ab}^{\rm int} + H_{ac}^{\rm int} + H_{bc}^{\rm int} + H_b^d + H_c^d, \quad (1)$$

where H_a, H_b, and H_c describe the free Hamiltonians of the microwave cavity mode, the Kittel mode, and the HMS mode, respectively, $H_{xy}^{\rm int}$ $(xy = ab, ac, bc)$ represents the interaction between the corresponding modes, and H_b^d (H_c^d) represents the coupling between the drive field and the Kittel (HMS) mode. It is worth noting that H_b, $H_{ab}^{\rm int}$, and H_b^d have forms similar to H_c, $H_{ac}^{\rm int}$, and H_c^d, so derivations of the latter will not be repeated here.

The free Hamiltonian of the cavity mode is

$$H_a = \frac{1}{2}\int \left(\epsilon_0 \mathbf{E}_a^2 + \frac{\mathbf{B}_a^2}{\mu_0}\right) d\tau, \quad (2)$$

where $\mathbf{E}_a$ $(\mathbf{B}_a)$ is the electric (magnetic) component of the electromagnetic field inside the cavity and ϵ_0 (μ_0) is the vacuum permittivity (permeability). By ignoring the constant term, the single-mode electromagnetic field can be quantized as $H_a = \hbar\omega_a \hat{a}^\dagger \hat{a}$, with $\hat{a}$ $(\hat{a}^\dagger)$ the annihilation (creation) operator of the photons at frequency ω_a [72].

The free Hamiltonian of the magnon mode, including the Zeeman energy and the magnetocrystalline anisotropy energy, can be written as [25]

$$H_b = -\int \mathbf{M}_b \cdot \mathbf{B}_0 d\tau - \frac{\mu_0}{2}\int \mathbf{M}_b \cdot \mathbf{H}_b^{\rm an} d\tau, \quad (3)$$

where $\mathbf{B}_0 = B_0 \mathbf{e}_z$ is the applied static magnetic field in the z direction for magnetizing the YIG sphere, with $\mathbf{e}_{i=x,y,z}$ the three orthogonal unit vectors [see Fig. 1(a)], and $\mathbf{M}_b = \hbar\gamma_g \mathbf{S}_b / V_{\rm YIG} \equiv (M_{\rm x}^b, M_{\rm y}^b, M_z^b)$ is the magnetization of the Kittel mode in the YIG sphere, with γ_g the gyromagnetic ratio [1], $V_{\rm YIG}$ the volume of the YIG sphere, and $\mathbf{S}_b \equiv (S_x^b, S_y^b, S_z^b)$ the collective spin operator of the Kittel mode. When the bias magnetic field is applied along the YIG sphere [100] crystal axis, the anisotropic field is given by [71,73]

$$\mathbf{H}_b^{\rm an} = \frac{2\hbar\gamma_g S_z^b K_{\rm an}^b}{\mu_0 M^2 V_{\rm YIG}} \mathbf{e}_z, \quad (4)$$

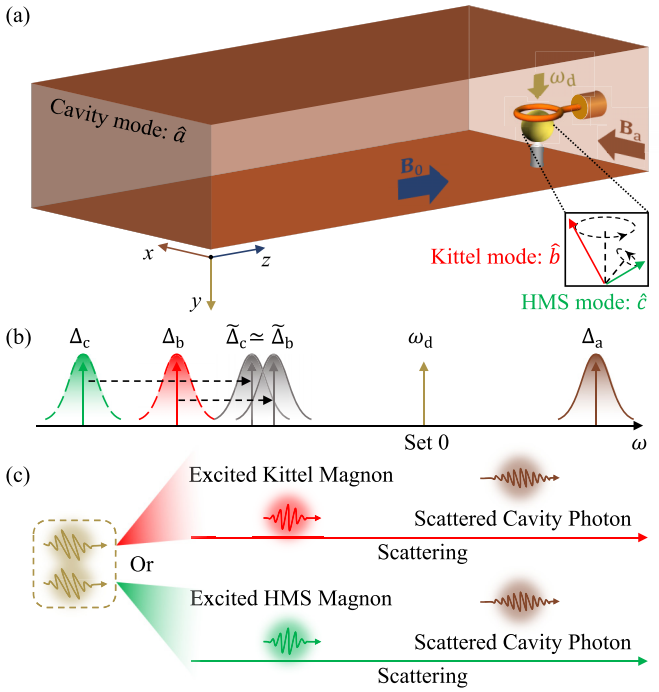

FIG. 1. (a) Sketch of the system (adapted from Ref. [66]). The YIG sphere is mounted on the cavity wall and magnetized to saturation by a bias magnetic field $\mathbf{B}_0$ in the z direction. The microwave source connected to the loop antenna provides a drive magnetic field, which is aligned along the y direction. The magnetic field of the microwave cavity is in the x direction. Three magnetic fields are mutually perpendicular at the position of the YIG sphere. The two magnetic moments represent the two spin-wave modes, respectively [the red (green) arrow corresponds to the Kittel (HMS) mode]. (b) Frequency spectrum of the cavity magnonic system. The existence of self-Kerr and cross-Kerr nonlinearities makes the microwave drive induce the effective frequency shift of the two magnon modes. When either the Kittel mode or the HMS mode is driven, the excess energy scatters photons with high frequency. If the cavity photon is matched with the frequency, the system exhibits all bipartite entanglements and genuine tripartite entanglement. (c) Four-wave mixing in cavity magnonics. If the cavity detuning in (b) is tuned to the matching condition ($\Delta_a = -\tilde{\Delta}_{b\,(c)}$), a four-wave mixing happens, where two driving photons are adsorbed and the cavity mode and the magnon mode are simultaneously excited

where $K_{\rm an}^b$ is the dominant first-order anisotropy coefficient and M is the saturation magnetization. The magnon-photon interaction Hamiltonian is

$$H_{ab}^{\rm int} = -\mu_0 \int \mathbf{M}_b \cdot \mathbf{B}_a d\tau, \quad (5)$$

where the magnetic field $\mathbf{B}_a = -(\hbar\omega_a/\mu_0 V_a)^{1/2}(\hat{a}^\dagger + \hat{a})\mathbf{e}_x$ of the cavity mode is polarized in the x direction, with V_a the volume of the cavity.

Due to the inhomogeneity of the bias magnetic field $\mathbf{B}_0$, HMS modes can occur in the YIG sphere. Here we consider one HMS mode near the Kittel mode in frequency. The interaction between the Kittel mode and the HMS mode can be

written as

$$H_{bc}^{\rm int} = \alpha \int \mathbf{M}_b \cdot \mathbf{M}_c d\tau, \tag{6}$$

with the coefficient α accounting for the overlap between these two spin-wave modes [66]. Here the magnetizations of the Kittel mode and the HMS mode are different ($\mathbf{M}_b \neq \mathbf{M}_c$) because more magnetic momentum is contributed to the Kittel mode.

The interaction Hamiltonian between the drive field and the Kittel mode is

$$H_b^d = -\mu_0 \int \mathbf{M}_b \cdot \mathbf{H}_d d\tau, \tag{7}$$

where $\mathbf{H}_d = iB_d \cos(\omega_d t)\mathbf{e}_y$ represents the drive field in the y direction, with drive frequency (amplitude) ω_d (B_d). For the low-lying magnon excitations with $\langle \hat{o}^\dagger \hat{o} \rangle \ll 2S_o$, where $o = b, c$, the Holstein-Primakoff transformations of the two modes are given by [74]

$$\begin{aligned} S_o^z &= S_o - \hat{o}^\dagger \hat{o}, \\ S_o^+ &= \hat{o}(2S_o - \hat{o}^\dagger \hat{o})^{1/2} \simeq (2S_o)^{1/2} \hat{o}, \\ S_o^- &= \hat{o}^\dagger (2S_o - \hat{o}^\dagger \hat{o})^{1/2} \simeq (2S_o)^{1/2} \hat{o}^\dagger, \end{aligned} \tag{8}$$

with $S_o^\pm \equiv S_o^x \pm i S_o^y$.

Under the rotating-wave approximation [72], the total effective Hamiltonian of the cavity magnonic system can be rewritten as

$$\begin{aligned} \frac{H}{\hbar} &= \omega_a \hat{a}^\dagger \hat{a} + \omega_b \hat{b}^\dagger \hat{b} + \omega_c \hat{c}^\dagger \hat{c} + K_b \hat{b}^\dagger \hat{b} \hat{b}^\dagger \hat{b} + K_c \hat{c}^\dagger \hat{c} \hat{c}^\dagger \hat{c} \\ &\quad + g_{ab}(\hat{a}^\dagger \hat{b} + \hat{a} \hat{b}^\dagger) + g_{ac}(\hat{a}^\dagger \hat{c} + \hat{a} \hat{c}^\dagger) + g_{bc}(\hat{b}^\dagger \hat{c} + \hat{b} \hat{c}^\dagger) \\ &\quad + G \hat{b}^\dagger \hat{b} \hat{c}^\dagger \hat{c} + \Omega_b (\hat{b}^\dagger e^{-i\omega_d t} - \hat{b} e^{i\omega_d t}) \\ &\quad + \Omega_c (\hat{c}^\dagger e^{-i\omega_d t} - \hat{c} e^{i\omega_d t}), \end{aligned} \tag{9}$$

where

$$\omega_{b\,(c)} = \gamma_g B_0 - \frac{2\hbar \gamma_g^2 K_{\rm an}^{b\,(c)} S_{b\,(c)}}{M^2 V_{\rm YIG}} - \frac{\alpha \hbar \gamma_g^2 S_{c\,(b)}}{V_{\rm YIG}} \tag{10}$$

is the angular frequency of the Kittel (HMS) mode,

$$K_{b\,(c)} = -\frac{\hbar \gamma_g^2 K_{\rm an}^{b\,(c)}}{M^2 V_{\rm YIG}}, \tag{11}$$

with $K_{\rm an}^{b\,(c)} < 0$, is the self-Kerr nonlinear coefficients of the Kittel (HMS) mode, and

$$g_{ab\,(ac)} = \sqrt{\frac{S_{b\,(c)} \gamma_g^2 \mu_0 \hbar \omega_a}{2V_a}} \tag{12}$$

denotes the coupling strength between the cavity mode and the Kittel (HMS) mode. Moreover, $g_{bc} = \alpha \hbar \gamma_g^2 (S_b S_c)^{1/2} / V_{\rm YIG}$ represents the coupling between the two magnon modes, $G = \alpha \hbar \gamma_g^2 / V_{\rm YIG}$ is the cross-Kerr coefficient, and $\Omega_{b\,(c)} = \frac{1}{4} \mu_0 \gamma_g B_d (2S_{b\,(c)})^{1/2}$ are the Rabi frequencies of the two spin-wave modes.

For the Kittel mode in a micrometer-scale YIG sphere, its spin moment contributes more to the dipole than that of the HMS mode [66]. Thus, we can reasonably ignore the coupling between the cavity mode and the HMS mode. Similarly, the beam-splitter-type interaction between the Kittel mode and the HMS mode is also small and hence can be neglected in the analysis. Then, in the rotating frame with respect to the drive frequency ω_d, the system Hamiltonian can be reduced to

$$\begin{aligned} \frac{H_{\rm eff}}{\hbar} &= \Delta_a \hat{a}^\dagger \hat{a} + \Delta_b \hat{b}^\dagger \hat{b} + \Delta_c \hat{c}^\dagger \hat{c} + K_b \hat{b}^\dagger \hat{b} \hat{b}^\dagger \hat{b} + K_c \hat{c}^\dagger \hat{c} \hat{c}^\dagger \hat{c} \\ &\quad + g_{ab}(\hat{a}^\dagger \hat{b} + \hat{a} \hat{b}^\dagger) + G \hat{b}^\dagger \hat{b} \hat{c}^\dagger \hat{c} + \Omega_b (\hat{b}^\dagger - \hat{b}) \\ &\quad + \Omega_c (\hat{c}^\dagger - \hat{c}), \end{aligned} \tag{13}$$

where $\Delta_{a\,(b,c)} = \omega_{a\,(b,c)} - \omega_d$.

III. DISSIPATIVE EQUATIONS AND COVARIANCE MATRIX

Due to the coupling between the cavity magnonic system and the environment, the system will inevitably be influenced by the cavity decay and magnetic damping. Taking these dissipative elements into account, the dissipative dynamics of the system is described by a set of quantum Langevin equations (QLEs)

$$\begin{aligned} \frac{d\hat{a}}{dt} &= -(i\Delta_a + \gamma_a)\hat{a} - i g_{ab} \hat{b} + (2\gamma_a)^{1/2} \hat{a}^{\rm in}, \\ \frac{d\hat{b}}{dt} &= -(i\Delta_b + \gamma_b)\hat{b} - i g_{ab} \hat{a} - i\Omega_b - iG \hat{b} \hat{c}^\dagger \hat{c} + (2\gamma_b)^{1/2} \hat{b}^{\rm in} \\ &\quad - 2iK_b \hat{b}^\dagger \hat{b} \hat{b}, \\ \frac{d\hat{c}}{dt} &= -(i\Delta_c + \gamma_c)\hat{c} - 2iK_c \hat{c}^\dagger \hat{c} \hat{c} - iG \hat{c} \hat{b}^\dagger \hat{b} - i\Omega_c \\ &\quad + (2\gamma_c)^{1/2} \hat{c}^{\rm in}, \end{aligned} \tag{14}$$

where γ_a, γ_b, and γ_c ($\hat{a}^{\rm in}$, $\hat{b}^{\rm in}$, and $\hat{c}^{\rm in}$) represent the damping rates (the zero-mean input noise operators) of the cavity mode, the Kittel mode, and the HMS mode, respectively. Under the Markovian reservoir assumption, the input noise operators are characterized by the correlation functions [75]

$$\begin{aligned} \langle \hat{o}^{\rm in\dagger}(t) \hat{o}^{\rm in}(t') \rangle &= n_o \delta(t - t'), \\ \langle \hat{o}^{\rm in}(t) \hat{o}^{\rm in\dagger}(t') \rangle &= (n_o + 1)\delta(t - t'), \end{aligned} \tag{15}$$

with $n_o = [\exp(\hbar\omega_o / k_B T_e) - 1]^{-1}$ the equilibrium mean thermal photon ($o = a$) and magnon ($o = b, c$) numbers. In addition, T_e is the environmental temperature and k_B is the Boltzmann constant. Because the YIG crystal is strongly driven by a microwave field, the couplings between different modes are unhindered, resulting in these modes all having large amplitudes (i.e., $|\langle o \rangle| \gg 1$), so the standard linearization treatment can be applied to the nonlinear QLEs (14). In this case, one can safely introduce the expansion $\hat{o} = \langle o \rangle + o$ in the vicinity of steady-state averages by neglecting higher-order fluctuations of the operators. Then we obtain a set of differential equations for mean values

$$\begin{aligned} \frac{d\langle a \rangle}{dt} &= -(i\Delta_a + \gamma_a)\langle a \rangle - i g_{ab} \langle b \rangle, \\ \frac{d\langle b \rangle}{dt} &= -(i\Delta_b + \gamma_b)\langle b \rangle - 2iK_b |\langle b \rangle|^2 \langle b \rangle - iG |\langle c \rangle|^2 \langle b \rangle \\ &\quad - i g_{ab} \langle a \rangle - i\Omega_b, \\ \frac{d\langle c \rangle}{dt} &= -(i\Delta_c + \gamma_c)\langle c \rangle - 2iK_c |\langle c \rangle|^2 \langle c \rangle - iG |\langle b \rangle|^2 \langle c \rangle - i\Omega_c. \end{aligned} \tag{16}$$

The steady-state solution of the system satisfies the equations

$$\begin{aligned} 0 &= -(i\Delta_b + \gamma_b)\langle b\rangle - 2iK_b|\langle b\rangle|^2\langle b\rangle - iG|\langle c\rangle|^2\langle b\rangle - i\Omega_b \\ &\quad - \frac{g_{ab}^2\langle b\rangle}{i\Delta_a + \gamma_a}, \\ 0 &= -(i\Delta_c + \gamma_c)\langle c\rangle - 2iK_c|\langle c\rangle|^2\langle c\rangle - iG|\langle b\rangle|^2\langle c\rangle - i\Omega_c. \end{aligned} \tag{17}$$

Supposing $|\Delta_a| \gg \gamma_a$, $|\Delta_b| \gg \gamma_b$, and $|\Delta_c| \gg \gamma_c$, we can approximately get that $\langle a\rangle$, $\langle b\rangle$, and $\langle c\rangle$ are all pure real numbers. It should be noted that the approximation is only used to demonstrate that $\langle a\rangle$, $\langle b\rangle$, and $\langle c\rangle$ are approximately real numbers, which simplifies the following calculations. However, the damping terms are included in all subsequent calculations and numerical simulations, which are necessary for the system to reach the steady state.

The linearized QLEs for the quantum fluctuations can be written as

$$\begin{aligned} \frac{da}{dt} &= -(i\Delta_a + \gamma_a)a - ig_{ab}b + (2\gamma_a)^{1/2}a^{\text{in}}, \\ \frac{db}{dt} &= -(i\tilde{\Delta}_b + \gamma_b)b - i\tilde{K}_b b^\dagger - ig_{ab}a - i\tilde{G}(c^\dagger + c) \\ &\quad + (2\gamma_b)^{1/2}b^{\text{in}}, \\ \frac{dc}{dt} &= -(i\tilde{\Delta}_c + \gamma_c)c - i\tilde{K}_c c^\dagger - i\tilde{G}(b^\dagger + b) + (2\gamma_c)^{1/2}c^{\text{in}}, \end{aligned} \tag{18}$$

where $\tilde{\Delta}_b = \Delta_b + 4K_b|\langle b\rangle|^2 + G|\langle c\rangle|^2$ and $\tilde{\Delta}_c = \Delta_c + 4K_c|\langle c\rangle|^2 + G|\langle b\rangle|^2$ are the effective magnon-mode–drive-field detunings including the frequency shifts caused by the self-Kerr and cross-Kerr effects. In addition, $\tilde{K}_b = 2K_b\langle b\rangle^2$ and $\tilde{K}_c = 2K_c\langle c\rangle^2$ are effective self-Kerr coefficients and $\tilde{G} = G\langle b\rangle\langle c\rangle$ is the effective magnon-magnon coupling rate. Since $\langle b\rangle$ and $\langle c\rangle$ are approximately pure real numbers, $\tilde{K}_b \simeq 2K_b|\langle b\rangle|^2$ and $\tilde{K}_c \simeq 2K_c|\langle c\rangle|^2$. In this case, we have $\tilde{\Delta}_b \simeq \Delta_b + 2\tilde{K}_b + G|\langle c\rangle|^2$ and $\tilde{\Delta}_c \simeq \Delta_c + 2\tilde{K}_c + G|\langle b\rangle|^2$.

In order to study the quantum correlation induced by the cross-Kerr effect, we first need to determine the cross-Kerr coefficient G. This can be done by using the parameters reported in the recent experiment in [66]. Due to the large frequency detuning between the Kittel mode and the HMS mode, the HMS mode is not excited when only the Kittel mode is driven (i.e., $\Omega_b \neq 0$ and $\Omega_c = 0$). In this case, the frequency shift ($2K_b|\langle b\rangle|^2/2\pi \simeq -60$ MHz) of the Kittel mode is caused by the self-Kerr nonlinearity, while the frequency shift ($G|\langle b\rangle|^2/2\pi \simeq -150$ MHz) of the HMS mode is due to the cross-Kerr effect. Therefore, $K_b/2\pi \simeq -0.1$ nHz (the bias magnetic field is applied along the YIG sphere [110] crystal axis), which corresponds to $G/2\pi \simeq -0.5$ nHz, can be found in a 1-mm-diam YIG sphere. Similarly, the Kittel mode is not excited when only the HMS mode is driven (i.e., $\Omega_c \neq 0$ and $\Omega_b = 0$). The frequency shift ($2K_c|\langle c\rangle|^2/2\pi \simeq -24$ MHz) of the HMS mode is caused by the self-Kerr nonlinearity, while the frequency shift ($G|\langle c\rangle|^2/2\pi \simeq -10$ MHz) of the Kittel mode is due to the cross-Kerr effect. So we can get $K_c/2\pi \simeq -0.6$ nHz.

TABLE I. Description of experimentally feasible parameters. Here MST denotes the maximum survival temperature. For related parameter detection, refer to Refs. [25,26,29,66].

Parameter	Value (all figures)
$\omega_a/2\pi$ (GHz)	Figs. 2–4, 10.07
$\omega_b/2\pi$ (GHz)	Figs. 2–4, 9.86
$\omega_c/2\pi$ (GHz)	Figs. 2–4, 9.7845
$\omega_d/2\pi$ (GHz)	Figs. 2–4, 9.97
$\Delta_a/2\pi$ (MHz)	Fig. 4, 100
$\Delta_b/2\pi$ (MHz)	Figs. 2–4, −110
$\Delta_c/2\pi$ (MHz)	Figs. 2–4, −185.5
$g_{ab}/2\pi$ (MHz)	Fig. 2, 35; Figs. 3 and 4, 30
$\gamma_a/2\pi$ (MHz)	Fig. 2, 5.5; Figs. 3 and 4, 18.6
$\gamma_b/2\pi$ (MHz)	Fig. 2, 12; Figs. 3 and 4, 6.7
$\gamma_c/2\pi$ (MHz)	Fig. 2, 12; Figs. 3 and 4, 6.7
$K_b/2\pi$ (nHz)	0.1 ([100] crystal axis)
$K_c/2\pi$ (nHz)	0.6 ([100] crystal axis)
$G/2\pi$ (nHz)	0.5 ([100] crystal axis)
$\tilde{K}_b/2\pi$ (MHz)	Fig. 2, 0; Fig. 3, 0, 7.5, 15; Fig. 4, 15
$\tilde{K}_c/2\pi$ (MHz)	Fig. 2, 0; Fig. 3, 0, 12, 24; Fig. 4, 24
$\tilde{\Delta}_b/2\pi$ (MHz)	Figs. 3 and 4, −70
$\tilde{\Delta}_c/2\pi$ (MHz)	Figs. 2–4, −100
$\tilde{G}/2\pi$ (MHz)	Figs. 2–4, 19.4
T_e (K)	Figs. 2 and 3, 0; Fig. 4, 0.15–0,2 (MST)

In this work we consider the following situation. The bias magnetic field is applied along the YIG sphere [100] crystal axis (i.e., $K_{b\,(c)}, G > 0$) and two drive fields are applied at the same time ($\Omega_{b\,(c)} \neq 0$), where $2K_b|\langle b\rangle|^2/2\pi \simeq 15$ MHz and $G|\langle b\rangle|^2/2\pi \simeq 37.5$ MHz correspond to $|\langle b\rangle|^2 \simeq 7.5 \times 10^{16}$, and $2K_c|\langle c\rangle|^2/2\pi \simeq 24$ MHz and $G|\langle c\rangle|^2/2\pi \simeq 10$ MHz correspond to $|\langle c\rangle|^2 \simeq 2 \times 10^{16}$. In this case, we have $\tilde{G}/2\pi \simeq 19.4$ MHz, which is utilized in the following analysis. More parameter details are listed in Table I. To quantify the entanglement of the system, we introduce the quadrature fluctuation (noise) operators $X_o = (o + o^\dagger)/\sqrt{2}$, $Y_o = i(o^\dagger - o)/\sqrt{2}$, $X_o^{\text{in}} = (o^{\text{in}} + o^{\text{in}\dagger})/\sqrt{2}$, and $Y_o^{\text{in}} = i(o^{\text{in}\dagger} - o^{\text{in}})/\sqrt{2}$, with $o = a, b, c$. The linearized QLEs (18) for the quadrature fluctuations can be written as

$$\begin{aligned} \frac{dX_a}{dt} &= \Delta_a Y_a - \gamma_a X_a + g_{ab}Y_b + (2\gamma_a)^{1/2}X_a^{\text{in}}, \\ \frac{dY_a}{dt} &= -\Delta_a X_a - \gamma_a Y_a - g_{ab}X_b + (2\gamma_a)^{1/2}Y_a^{\text{in}}, \\ \frac{dX_b}{dt} &= (\tilde{\Delta}_b - \tilde{K}_b)Y_b - \gamma_b X_b + g_{ab}Y_a + (2\gamma_b)^{1/2}X_b^{\text{in}}, \\ \frac{dY_b}{dt} &= -(\tilde{\Delta}_b + \tilde{K}_b)X_b - \gamma_b Y_b - g_{ab}X_a - 2\tilde{G}X_c + (2\gamma_b)^{1/2}Y_b^{\text{in}}, \\ \frac{dX_c}{dt} &= (\tilde{\Delta}_c - \tilde{K}_c)Y_c - \gamma_c X_c + (2\gamma_c)^{1/2}X_c^{\text{in}}, \\ \frac{dY_c}{dt} &= -(\tilde{\Delta}_c + \tilde{K}_c)X_c - \gamma_c Y_c - 2\tilde{G}X_b + (2\gamma_c)^{1/2}Y_c^{\text{in}}. \end{aligned} \tag{19}$$

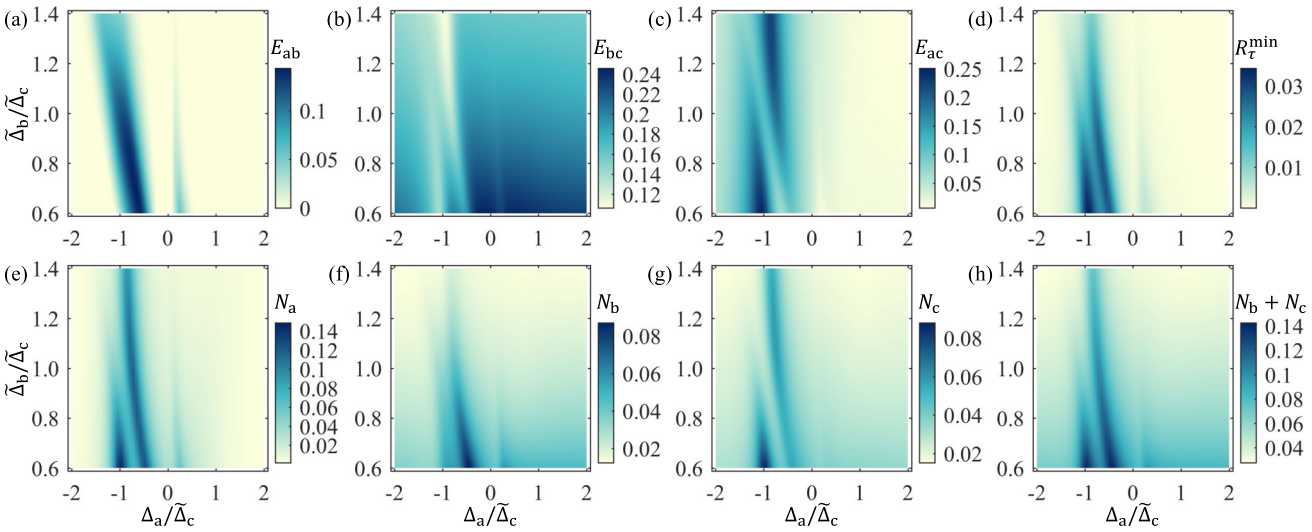

FIG. 2. Bipartite entanglements (a) E_{ab}, (b) E_{bc}, and (c) E_{ac} and (d) tripartite entanglement $R_\tau^{\min}$ versus detunings $\tilde{\Delta}_b$ and Δ_a. Mean excitation numbers for (e) the cavity mode N_a, (f) the Kittel mode N_b, (g) the HMS mode N_c, and (h) the sum of N_b and N_c versus $\tilde{\Delta}_b$ and Δ_a. See Table I for the detailed parameters.

Then Eqs. (19) can be expressed in a more concise form

$$\frac{du}{dt} = Au(t) + v(t), \tag{20}$$

where the drift matrix A reads

$$A = \begin{pmatrix} -\gamma_a & \Delta_a & 0 & g_{ab} & 0 & 0 \\ -\Delta_a & -\gamma_a & -g_{ab} & 0 & 0 & 0 \\ 0 & g_{ab} & -\gamma_b & \tilde{\Delta}_b - \tilde{K}_b & 0 & 0 \\ -g_{ab} & 0 & -\tilde{\Delta}_b - \tilde{K}_b & -\gamma_b & -2\tilde{G} & 0 \\ 0 & 0 & 0 & 0 & -\gamma_c & \tilde{\Delta}_c - \tilde{K}_c \\ 0 & 0 & -2\tilde{G} & 0 & -\tilde{\Delta}_c - \tilde{K}_c & -\gamma_c \end{pmatrix} \tag{21}$$

and $u = [X_a, Y_a, X_b, Y_b, X_c, Y_c]^T$ and $v = [(2\gamma_a)^{1/2}X_a^{\rm in}, (2\gamma_a)^{1/2}Y_a^{\rm in}, (2\gamma_b)^{1/2}X_b^{\rm in}, (2\gamma_b)^{1/2}Y_b^{\rm in}, (2\gamma_c)^{1/2}X_c^{\rm in}, (2\gamma_c)^{1/2}Y_c^{\rm in}]^T$ are the vectors for quantum fluctuations and noises, respectively. Since the dynamics of the system is governed by a set of linearized QLEs, the Gaussian nature of the input states will be preserved during the time evolution. That is, the steady state of the quantum fluctuations of the system is a CV three-mode Gaussian state. The state can be fully characterized by a stationary covariance matrix (CM) V whose matrix element is defined by

$$V_{ij} = \tfrac{1}{2}\langle u_i(t)u_j(t') + u_j(t')u_i(t)\rangle, \tag{22}$$

with $i, j = 1, 2, \ldots, 6$. The matrix V is obtained by solving the Lyapunov equation [53,76]

$$\frac{dV}{dt} = A(t)V(t) + V(t)A^T(t) + D, \tag{23}$$

where $D = \text{diag}[\gamma_a(2n_a + 1), \gamma_a(2n_a + 1), \gamma_b(2n_b + 1), \gamma_b(2n_b + 1), \gamma_c(2n_c + 1), \gamma_c(2n_c + 1)]$ is a diffusion matrix and whose matrix element is related to the noise correlations and defined by

$$D_{ij} = \frac{\langle v_i(t)v_j(t') + v_j(t')v_i(t)\rangle}{2\delta(t - t')}. \tag{24}$$

To study the bipartite CV entanglements, we introduce the logarithmic negativity E_N (which includes E_{ab}, cavity-Kittel entanglement; E_{ac}, cavity-HMS entanglement; and E_{bc}, Kittel-HMS entanglement). Further, for the tripartite entanglement, we use the minimum residual contangle $R_\tau^{\min}$, whose definition can be found in the Appendix, which includes Refs. [52,77–79].

IV. ENTANGLED STATE GENERATION VIA THE CROSS-KERR EFFECT

In order to show the behavior of the entanglements induced by the cross-Kerr effect, Figs. 2(a)–2(d) describe bipartite entanglements E_{ab} [Fig. 2(a)], E_{ac} [Fig. 2(b)], and E_{bc} [Fig. 2(c)] and tripartite entanglement [Fig. 2(d)] $R_\tau^{\min}$ as a function of two detunings $\tilde{\Delta}_b$ and Δ_a, where the two self-Kerr effects are not considered. In fact, the self-Kerr effects of the two modes

can be characterized by their magnetocrystalline anisotropy energies, which are defined as [57]

$$\frac{\mathcal{E}_{b\,(c)}}{\hbar} = -\frac{2\gamma_g S_z^{b\,(c)} M_z^{b\,(c)} K_{\rm an}^{b\,(c)}}{M^2}. \tag{25}$$

The energies may be eliminated by adjusting the angle between the bias magnetic field and the crystal axis [73]. According to the Routh-Hurwitz criterion, the system is stable and reaches its steady state when all the eigenvalues of the matrix A have negative real parts. Therefore, we start our analysis by determining the eigenvalues of the matrix A (i.e., $|A - \lambda \mathbf{I}| = 0$) and make sure that the stability conditions are all satisfied in numerical simulations. The parameters used in the article are shown in Table I, which are adopted from the experimental studies in Refs. [25,26,29,66].

As illustrated in Fig 2(b), the entanglement E_{bc} emerges when $\tilde{\Delta}_b \simeq \tilde{\Delta}_c$. However, when the spin-wave subsystems are near-resonantly coupled to the cavity field, that is, when $\Delta_a \simeq -\tilde{\Delta}_c$, E_{bc} is partially transferred to cavity-mode–Kittel-mode and cavity-mode–HMS-mode subsystems. As a result, entanglements E_{ab} and E_{ac} arise, as shown in Figs. 2(a) and 2(c). At the same time, the tripartite entanglement of the system can be generated [see Fig. 2(d)]. The physics behind the scenes are as follows. The two magnon modes (the Kittel mode and the HMS mode) are initially detuned and can be driven strongly by the microwave source. Due to the existence of the self-Kerr and cross-Kerr effects, two magnon modes can be driven close to resonance. We begin by demonstrating the situation in the absence of two self-Kerr effects, which is necessary to elucidate the condition for optimizing magnon-magnon entanglement solely through cross-Kerr nonlinearity. Then we proceed to analyze the quantum fluctuations via the linearized Hamiltonian

$$\frac{H_{\rm flu}}{\hbar} = \Delta_a a^\dagger a + \tilde{\Delta}_b b^\dagger b + \tilde{\Delta}_c c^\dagger c + \tilde{G}(b^\dagger + b)(c^\dagger + c) + g_{ab}(a^\dagger b + a b^\dagger), \tag{26}$$

where $\tilde{G}(b^\dagger c^\dagger + bc)$ implies the two-mode-squeezing-type interaction between the Kittel mode and the HMS mode induced by the cross-Kerr effect, which can be significantly enhanced by driving the magnon modes. The Hamiltonian (26) describes the magnon-magnon entanglement when $\tilde{G} \neq 0$. If the cavity field is further participated in the entanglement production and scattering, the four-wave mixing gives rises to the magnon-mode–cavity-mode entanglement [see Figs. 1(b) and 1(c)]. The spontaneous parametric process leads to the transfer of entanglement at suitable detuning frequencies (i.e., matching condition: $\Delta_a \simeq -\tilde{\Delta}_{b\,(c)}$). In this case, the indirectly coupled cavity photons and HMS-mode magnons get entangled and the entanglement is even larger than those in directly coupled subsystems [see Figs. 2(b) and 2(c) for $\Delta_a = -\tilde{\Delta}_{b\,(c)}$]. A similar mechanism with three-wave mixing has also been found in optomechanical systems [54] and cavity magnetomechanical systems [21]. It is worth noting that the split structures in Fig. 2 are a feature of the entanglement distribution among three bipartite subsystems. A similar characteristic was shown in Fig. 2 of Ref. [21], but due to the more involved dynamics in our system, the complementary distribution of the entanglement is not as clearly visible as in Ref. [21].

To demonstrate the conversion process, we introduce the final mean photon and magnon numbers, which can be calculated by the relation

$$N_o = \tfrac{1}{2}\left(\langle X_o^2\rangle + \langle Y_o^2\rangle - 1\right), \tag{27}$$

where $o = a, b, c$ correspond to the excitation numbers of the cavity mode, the Kittel mode, and the HMS mode, respectively. Figures 2(e)–2(h) present the excitation numbers N_a [Fig. 2(e)], N_b [Fig. 2(f)], N_c [Fig. 2(g)], and $N_b + N_c$ [Fig. 2(h)] as a function of the two detunings of $\tilde{\Delta}_b$ and Δ_a, where two self-Kerr effects are not considered. The numerical results are carried out in a zero-temperature environment ($T_e = 0$ K) and a strong-coupling regime ($g_{ab}, \tilde{G} > \gamma_a, \gamma_b, \gamma_c$), where the dissipation rate for each mode is chosen from experimentally feasible parameters. All the parameters ensure that the system is always stable. We can find that the frequency ranges of the excited two magnon modes are complementary [see Figs. 2(f) and 2(g)]. Here $N_a \simeq N_b + N_c$ implies that no matter which magnon mode is excited, it is accompanied by the scattering of microwave photons [see Figs. 2(e) and 2(h)]. The schematic diagram corresponding to the numerical results in Fig. 2 is shown in Figs. 1(b) and 1(c), where the matching condition of parametric conversion process determines the optimal frequency detunings at which cavity photons can be entangled.

V. SELF-KERR EFFECT INDUCED ENTANGLED STATE TRANSFER

In fact, it is unavoidable that the effective self-Kerr effects will also be enhanced when the YIG sphere is pumped by the drive field. This is a problem that the majority of entanglement generation schemes avoid, namely, the presence of multiple nonlinearities in the system. Numerous nonlinear combined effects contribute to the system's difficulty of analysis and instability. However, we demonstrate in this article that the presence of self-Kerr effects enhances magnon-magnon entanglement transfer into other subsystems, resulting in a significant increase in tripartite entanglements. Figure 3 describes bipartite entanglements E_{ab} [Fig. 3(a)], E_{bc} [Fig. 3(b)], and E_{ac} [Fig. 3(c)] and tripartite entanglement $R_\tau^{\rm min}$ [Fig. 3(d)] as a function of the detuning Δ_a for different self-Kerr coefficients, where a lower cavity-mode–Kittel-mode coupling rate $g_{ab}/2\pi = 30$ MHz is chosen for better illustration. Figure 3(b) shows that when $\Delta_a \simeq -\tilde{\Delta}_c$, E_{bc} decreases gradually as two self-Kerr coefficients increase. Instead, E_{ab} and E_{ac} gradually increase in the process [see Figs. 3(a) and 3(c)], which implies that more entanglement in the Kittel-mode–HMS-mode subsystem is transferred to the cavity-mode–Kittel-mode and cavity-mode–HMS-mode subsystems. The tripartite entanglement in terms of the minimum residual contangle becomes stronger when the entanglement is more evenly distributed in each subsystem, as illustrated in Fig. 3(d).

When the two self-Kerr effects are considered, the linearized Hamiltonian of the system can be rewritten as

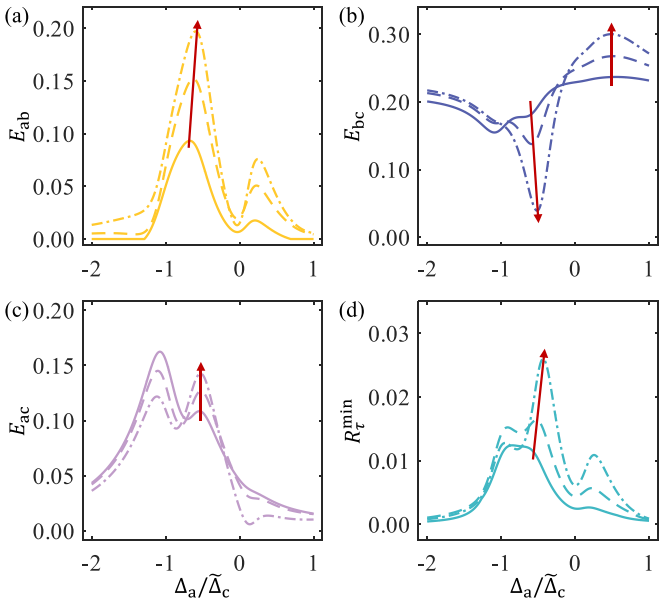

FIG. 3. Bipartite entanglements (a) E_{ab}, (b) E_{bc}, and (c) E_{ac} and tripartite entanglement (d) $R_\tau^{\min}$ versus Δ_a for different self-Kerr coefficients $\tilde{K}_b$ and $\tilde{K}_c$. We take $\tilde{K}_b = \tilde{K}_c = 0$ (solid line), $\tilde{K}_b/2\pi = 7.5$ MHz and $\tilde{K}_c/2\pi = 12$ MHz (dashed line), and $\tilde{K}_b/2\pi = 15$ MHz and $\tilde{K}_c/2\pi = 24$ MHz (dot-dashed line). The arrows depict the evolution of the entanglement as the two self-Kerr effects are enhanced. The other parameters are listed in Table I.

$$\frac{H_L}{\hbar} = \Delta_a a^\dagger a + \tilde{\Delta}_b b^\dagger b + \tilde{\Delta}_c c^\dagger c + g_{ab}(a^\dagger b + a b^\dagger) + \frac{\tilde{K}_b(b^\dagger b^\dagger + bb)}{2} + \frac{\tilde{K}_c(c^\dagger c^\dagger + cc)}{2} + \tilde{G}(b^\dagger + b)(c^\dagger + c). \tag{28}$$

To show the mechanism, we diagonalize these two terms by introducing squeezing operators

$$S(\theta_b) = \exp[\theta_b(bb - b^\dagger b^\dagger)],$$
$$S(\theta_c) = \exp[\theta_c(cc - c^\dagger c^\dagger)]. \tag{29}$$

The two Bogoliubov modes can be written as

$$\beta_b = S^\dagger(\theta_b) b S(\theta_b) = \cosh\theta_b b - \sinh\theta_b b^\dagger,$$
$$\beta_c = S^\dagger(\theta_c) c S(\theta_c) = \cosh\theta_c c - \sinh\theta_c c^\dagger, \tag{30}$$

where

$$\theta_{b\,(c)} = \tfrac{1}{4}\ln C_{b\,(c)}, \tag{31}$$

with

$$C_{b\,(c)} = \frac{\tilde{\Delta}_{b\,(c)} - \tilde{K}_{b\,(c)}}{\tilde{\Delta}_{b\,(c)} + \tilde{K}_{b\,(c)}}.$$

For simplicity, we set $\tilde{\Delta}_b \simeq \tilde{\Delta}_c \simeq \tilde{\Delta}$ and $\tilde{K}_b \simeq \tilde{K}_c \simeq \tilde{K}$, so $C_b \simeq C_c \simeq C$ and $\theta_b \simeq \theta_c \simeq \theta$. In fact, $|\tilde{\Delta}_b| < |\tilde{\Delta}_c|$ and $\tilde{K}_b < \tilde{K}_c$, but the above setting does not lose the generality of the analysis. Therefore, the Bogoliubov Hamiltonian can be written as

$$\frac{H_B}{\hbar} = \Delta_a a^\dagger a + \Delta_\beta \beta_b^\dagger \beta_b + \Delta_\beta \beta_c^\dagger \beta_c + \mathcal{G}(\beta_b + \beta_b^\dagger)(\beta_c + \beta_c^\dagger) + g_{ab}^{\cos}(\beta_b^\dagger a + \beta_b a^\dagger) + g_{ab}^{\sin}(\beta_b^\dagger a^\dagger + \beta_b a), \tag{32}$$

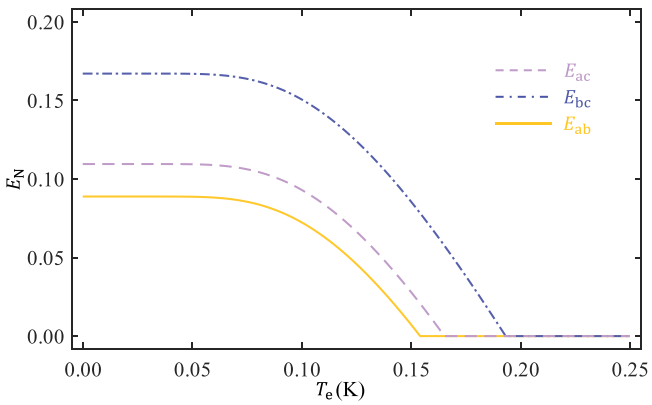

FIG. 4. Bipartite entanglements E_{ab}, E_{bc}, and E_{ac} versus environmental temperature T_e. See Table I for the the parameters.

where $g_{ab}^{\cos} = g_{ab}\cosh\theta$, $g_{ab}^{\sin} = g_{ab}\sinh\theta$, $\Delta_\beta = (\tilde{\Delta}^2 - \tilde{K}^2)^{1/2}$, and $\mathcal{G} = \tilde{G}\sqrt{C}$. Equation (32) shows that $\Delta_a \simeq -\Delta_\beta$ is optimal for the cavity-mode–Kittel-mode entanglement, due to the squeezing term $g_{ab}^{\sin}(\beta_b^\dagger a^\dagger + \beta_b a)$, which also results in a frequency shift for optimal detuning. In fact, when self-Kerr nonlinearity is introduced, the entanglement E_{bc} becomes stronger because $C > 1$ [see Fig. 3(b) for $\Delta_a \not\simeq -\tilde{\Delta}_c$]. At the same time, the cavity-mode–Kittel-mode state-swap interaction is also enhanced because $g_{ab}^{\cos} > g_{ab}$ for $\theta \neq 0$. Thus, the enhancement of E_{ab} and E_{ac} has two causes: (i) more entanglement being transferred into the subsystem containing the cavity mode [see Figs. 3(a)–3(c)] and (ii) the emergence of a new two-mode-squeezing term $g_{ab}^{\sin}(\beta_b^\dagger a^\dagger + \beta_b a)$. The results show that the self-Kerr effect facilitates the transfer of entanglement, which can make the minimum residual contangle $R_\tau^{\min}$ larger than the previous value [see Fig. 3(d) for $\Delta_a \simeq -\tilde{\Delta}_c$]. Finally, the generated subsystem entanglements are robust against environmental temperature and the maximum survival temperature is about 0.15–0.2 K, as shown in Fig. 4.

VI. ENTANGLEMENT DETECTION AND APPLICATION

The generated magnon-magnon entanglement can be detected by measuring the quadratures of the two magnon modes $X_{b\,(c)}$ and $Y_{b\,(c)}$ and then calculating the covariance matrix. The entanglement parameter region shown Fig. 2 shows that entanglement can be obtained even when there is certain frequency detuning between the two magnon modes. Two weak microwave probe fields resonantly coupled to the two detuned magnon modes can read out the four quadratures by using the cavity-magnon beam-splitter interaction. Here we focus on the detection of magnon-magnon entanglement E_{bc}. To achieve the entanglement detection, the dissipation rate of two magnon modes should be much lower than that of the cavity mode (e.g., we take $\gamma_a/2\pi = 18.6$ MHz and $\gamma_{b\,(c)}/2\pi = 6.7$ MHz in Fig. 3). As a result, when the pump tone is turned off, cavity microwave photons dissipate quickly. We send the two probe fields after the cavity photons dissipate completely. Then the probe output fields contain only the information regarding the entanglement of the two magnon modes.

Quantum entanglement is a phenomenon wherein systems cannot be described independently of one another despite being separated by an arbitrarily large distance. It is also the key resource behind many emerging quantum technologies, such as quantum computing [42–45] and metrology [46,47]. The entanglement of two different degrees of freedom inside one ferrimagnetic crystal provides a concept for CV information processing at the mesoscopic scale. Our research sheds light on the entanglement scheme between additional HMS modes and Kittel mode induced by their nonlinear couplings.

VII. CONCLUSION

In summary, we have presented a scheme to generate steady-state entanglement in a cavity magnonic system where a microwave cavity mode is coupled to a Kittel mode in a YIG sphere and the Kittel mode is simultaneously coupled to a HMS mode via mode overlap, which originates from the partial local spins shared by the Kittel mode and other spin-wave modes [70,71]. In such a system, we studied the properties of entangled magnon modes and found that the cross-Kerr effect is able to induce steady-state entanglement between two magnon modes with experimentally accessible parameters. Additionally, when the spontaneous parametric process occurs, the cavity photons also become entangled with the magnons. We also demonstrated the effect of the self-Kerr nonlinearities on the bipartite and tripartite entanglements, where the mutual coupling between different modes becomes stronger and a new two-mode squeezed state is generated. When the two types of nonlinearities coexist, the entanglement is more uniformly distributed across the subsystems and the tripartite entanglement is also enhanced.

Our work will open up different avenues for studying entanglement when multiple nonlinearities exist, as well as for realizing an entangled state within a single YIG sphere, which will enable spatially localized conservation of entanglement in ferrimagnetic spin ensembles. Moreover, the method for generating steady-state entanglement via the cross-Kerr effect could be extended to other hybrid systems. In quantum magnonic systems [9], a cross-Kerr nonlinear interaction between the magnetostatic mode and the qubit is also facilitated by their mutual couplings to microwave cavity modes [80,81], which provides the additional nonlinearity required to investigate quantum effects in magnonics.

ACKNOWLEDGMENTS

This work was supported by the National Natural Science Foundation of China (Grants No. 11934010, No. U1801661, and No. 12174329), Zhejiang Province Program for Science and Technology (Grant No. 2020C01019), and the Fundamental Research Funds for the Central Universities (Grant No. 2021FZZX001-02).

APPENDIX: QUANTIFICATION OF ENTANGLEMENTS

Here we briefly give the quantification of the bipartite and tripartite entanglements. To study the bipartite CV entanglements, we introduce the logarithmic negativity, which is defined as [77,78]

$$E_N = \max[0, -\ln(2\nu^-)], \tag{A1}$$

where $\nu^- = \min|\mathrm{eig}\oplus_{s=1}^{2}(-\sigma_y)P_{1|2}V_4P_{1|2}|$, with σ_y the Pauli y matrix. Here V_4 is the 4×4 CM of the two subsystems that only includes the rows and columns of the interested modes in V, and the matrix $P_{1|2} = \sigma_z \oplus \mathbb{1}$ (with the identity matrix $\mathbb{1}$) realizes partial transposition at the CM level. In the main text, we use E_{ab}, E_{ac}, and E_{bc} to denote the cavity-mode–Kittel-mode, the cavity-mode–HMS mode, and the Kittel-mode–HMS-mode entanglements, respectively.

To investigate the tripartite CV entanglement, we introduce a residual contangle defined as [52,79]

$$R_\tau^{i|jk} = C_{i|jk} - C_{i|j} - C_{i|k}, \tag{A2}$$

with $i, j, k = a, b, c$. In addition, $C_{m|n} = E_{m|n}^2$, as the squared logarithmic negativity with entanglement monotonicity, is the contangle of m and n subsystems, where n may involve one or two modes. The single-mode versus dual-mode logarithmic negativity is defined as

$$E_{i|jk} = \max[0, -\ln(2\nu_{i|jk}^-)], \tag{A3}$$

where $\nu_{i|jk}^- = \min|\mathrm{eig}i\oplus_{s=1}^{3}(i\sigma_y)\tilde{V}|$ is the minimum symplectic eigenvalue of the 6×6 CM $\tilde{V} = P_{i|jk}VP_{i|jk}$. The matrices $P_{1|23} = \sigma_z \oplus \mathbb{1} \oplus \mathbb{1}$, $P_{2|13} = \mathbb{1} \oplus \sigma_z \oplus \mathbb{1}$, and $P_{3|12} = \mathbb{1} \oplus \mathbb{1} \oplus \sigma_z$ are used for partial transposition at the level of the full CM. Here $R_\tau^{i|jk} \geqslant 0$ implies that the residue contangle R_τ satisfies the quantum entanglement monogamy. The minimum residual contangle is defined as [52,79]

$$R_\tau^{\min} = \min\left[R_\tau^{a|bc}, R_\tau^{b|ac}, R_\tau^{c|ab}\right], \tag{A4}$$

which characterizes a *bona fide* three-party property of the CV three-mode Gaussian states.

[1] Ö. O. Soykal and M. E. Flatté, Strong Field Interactions between a Nanomagnet and a Photonic Cavity, Phys. Rev. Lett. **104**, 077202 (2010).

[2] H. Huebl, C. W. Zollitsch, J. Lotze, F. Hocke, M. Greifenstein, A. Marx, R. Gross, and S. T. B. Goennenwein, High Cooperativity in Coupled Microwave Resonator Ferrimagnetic Insulator Hybrids, Phys. Rev. Lett. **111**, 127003 (2013).

[3] Y. Tabuchi, S. Ishino, T. Ishikawa, R. Yamazaki, K. Usami, Y. Nakamura, Hybridizing Ferromagnetic Magnons and Microwave Photons in the Quantum Limit, Phys. Rev. Lett. **113**, 083603 (2014).

[4] X. Zhang, C.-L. Zou, L. Jiang, and H. X. Tang, Strongly Coupled Magnons and Cavity Microwave Photons, Phys. Rev. Lett. **113**, 156401 (2014).

[5] M. Goryachev, W. G. Farr, D. L. Creedon, Y. Fan, M. Kostylev, and M. E. Tobar, High-Cooperativity Cavity QED with Magnons at Microwave Frequencies, Phys. Rev. Applied **2**, 054002 (2014).

[6] L. Bai, M. Harder, Y. P. Chen, X. Fan, J. Q. Xiao, and C.-M. Hu, Spin Pumping in Electrodynamically Coupled Magnon-Photon Systems, Phys. Rev. Lett. **114**, 227201 (2015).

[7] Y. Cao, P. Yan, H. Huebl, S. T. B. Goennenwein, and G. E. W. Bauer, Exchange magnon-polaritons in microwave cavities, Phys. Rev. B **91**, 094423 (2015).

[8] D. Zhang, X.-M. Wang, T.-F. Li, X.-Q. Luo, W. Wu, F. Nori, and J. Q. You, Cavity quantum electrodynamics with ferromagnetic magnons in a small yttrium-iron-garnet sphere, npj Quantum Inf. **1**, 15014 (2015).

[9] D. Lachance-Quirion, Y. Tabuchi, A. Gloppe, K. Usami, and Y. Nakamura, Hybrid quantum systems based on magnonics, Appl. Phys. Express **12**, 070101 (2019).

[10] B. Z. Rameshti, S. V. Kusminskiy, J. A. Haigh, K. Usami, D. Lachance-Quirion, Y. Nakamura, C.-M. Hu, H. X. Tang, G. E. W. Bauer, and Y. M. Blanter, Cavity magnonics, arXiv:2106.09312.

[11] H. Y. Yuan, Y. Cao, A. Kamra, R. A. Duine, and P. Yan, Quantum magnonics: When magnon spintronics meets quantum information science, Phys. Rep. **965**, 1 (2022).

[12] Y.-R. Shen and N. Bloembergen, Interaction between light waves and spin waves, Phys. Rev. **143**, 372 (1966).

[13] R. Hisatomi, A. Osada, Y. Tabuchi, T. Ishikawa, A. Noguchi, R. Yamazaki, K. Usami, and Y. Nakamura, Bidirectional conversion between microwave and light via ferromagnetic magnons, Phys. Rev. B **93**, 174427 (2016).

[14] A. Osada, R. Hisatomi, A. Noguchi, Y. Tabuchi, R. Yamazaki, K. Usami, M. Sadgrove, R. Yalla, M. Nomura, and Y. Nakamura, Cavity Optomagnonics with Spin-Orbit Coupled Photons, Phys. Rev. Lett. **116**, 223601 (2016).

[15] X. Zhang, N. Zhu, C.-L. Zou, and H. X. Tang, Optomagnonic Whispering Gallery Microresonators, Phys. Rev. Lett. **117**, 123605 (2016).

[16] A. Osada, A. Gloppe, R. Hisatomi, A. Noguchi, R. Yamazaki, M. Nomura, Y. Nakamura, and K. Usami, Brillouin Light Scattering by Magnetic Quasivortices in Cavity Optomagnonics, Phys. Rev. Lett. **120**, 133602 (2018).

[17] Y. Tabuchi, S. Ishino, A. Noguchi, T. Ishikawa, R. Yamazaki, K. Usami, and Y. Nakamura, Coherent coupling between a ferromagnetic magnon and a superconducting qubit, Science **349**, 405 (2015).

[18] Y. Tabuchi, S. Ishino, A. Noguchi, T. Ishikawa, R. Yamazaki, K. Usami, and Y. Nakamura, Quantum magnonics: The magnon meets the superconducting qubit, C. R. Phys. **17**, 729 (2016).

[19] D. Lachance-Quirion, Y. Tabuchi, S. Ishino, A. Noguchi, T. Ishikawa, R. Yamazaki, and Y. Nakamura, Resolving quanta of collective spin excitations in a millimeter-sized ferromagnet, Sci. Adv. **3**, e1603150 (2017).

[20] X. Zhang, C.-L. Zou, L. Jiang, and H. X. Tang, Cavity magnomechanics, Sci. Adv. **2**, e1501286 (2016).

[21] J. Li, S.-Y. Zhu, and G. S. Agarwal, Magnon-Photon-Phonon Entanglement in Cavity Magnomechanics, Phys. Rev. Lett. **121**, 203601 (2018).

[22] J. Li, S.-Y. Zhu, and G. S. Agarwal, Squeezed states of magnons and phonons in cavity magnomechanics, Phys. Rev. A **99**, 021801(R) (2019).

[23] J. Li and S.-Y. Zhu, Entangling two magnon modes via magnetostrictive interaction, New J. Phys. **21**, 085001 (2019).

[24] X. Zhang, C.-L. Zou, N. Zhu, F. Marquardt, L. Jiang, and H. X. Tang, Magnon dark modes and gradient memory, Nat. Commun. **6**, 8914 (2015).

[25] Y.-P. Wang, G.-Q. Zhang, D. Zhang, X.-Q. Luo, W. Xiong, S.-P. Wang, T.-F. Li, C.-M. Hu, and J. Q. You, Magnon Kerr effect in a strongly coupled cavity-magnon system, Phys. Rev. B **94**, 224410 (2016).

[26] Y.-P. Wang, G.-Q. Zhang, D. Zhang, T.-F. Li, C.-M. Hu, and J. Q. You, Bistability of Cavity Magnon Polaritons, Phys. Rev. Lett. **120**, 057202 (2018).

[27] M. Harder, L. Bai, P. Hyde, and C.-M. Hu, Topological properties of a coupled spin-photon system induced by damping, Phys. Rev. B **95**, 214411 (2017).

[28] D. Zhang, X.-Q. Luo, Y.-P. Wang, T.-F. Li, and J. Q. You, Observation of the exceptional point in cavity magnonpolaritons, Nat. Commun. **8**, 1368 (2017).

[29] Y.-P. Wang, J. W. Rao, Y. Yang, P.-C. Xu, Y. S. Gui, B. M. Yao, J. Q. You, and C.-M. Hu, Nonreciprocity and Unidirectional Invisibility in Cavity Magnonics, Phys. Rev. Lett. **123**, 127202 (2019).

[30] Y.-P. Wang and C.-M. Hu, Dissipative couplings in cavity magnonics, J. Appl. Phys. **127**, 130901 (2020).

[31] J. Zhao, Y. Liu, L. Wu, C.-K. Duan, Y.-x. Liu, and J. Du, Observation of Anti-$\mathcal{PT}$-Symmetry Phase Transition in the Magnon-Cavity-Magnon Coupled System, Phys. Rev. Applied **13**, 014053 (2020).

[32] Y. Yang, Y.-P. Wang, J. W. Rao, Y. S. Gui, B. M. Yao, W. Lu, and C.-M. Hu, Unconventional Singularity in Anti-Parity-Time Symmetric Cavity Magnonics, Phys. Rev. Lett. **125**, 147202 (2020).

[33] B. Wang, Z.-X. Liu, C. Kong, H. Xiong, and Y. Wu, Magnon induced transparency and amplification in $\mathcal{PT}$-symmetric cavity magnon system, Opt. Express **26**, 20248 (2018).

[34] Z. Zhang, M. O. Scully, and G. S. Agarwal, Quantum entanglement between two magnon modes via Kerr nonlinearity driven far from equilibrium, Phys. Rev. Research **1**, 023021 (2019).

[35] H. Y. Yuan, S. Zhang, Z. Ficek, Q. Y. He, and M.-H. Yung, Enhancement of magnon-magnon entanglement inside a cavity, Phys. Rev. B **101**, 014419 (2020).

[36] H. . Yuan, P. Yan, S. Zheng, Q. Y. He, K. Xia, and M.-H. Yung, Steady Bell State Generation via Magnon-Photon Coupling, Phys. Rev. Lett. **124**, 053602 (2020).

[37] J. M. P. Nair and G. S. Agarwal, Deterministic quantum entanglement between macroscopic ferrite samples, Appl. Phys. Lett. **117**, 084001 (2020).

[38] M. Elyasi, Y. M. Blanter, and G. E. W. Bauer, Resources of nonlinear cavity magnonics for quantum information, Phys. Rev. B **101**, 054402 (2020).

[39] Z.-B. Yang, X.-D. Liu, X.-Y. Yin, Y. Ming, H.-Y. Liu, and R.-C. Yang, Controlling Stationary One-Way Quantum Steering in Cavity Magnonics, Phys. Rev. Applied **15**, 024042 (2021).

[40] Z.-B. Yang, H. Jin, J.-W. Jin, J.-Y. Liu, H.-Y. Liu, and R.-C. Yang, Bistability of squeezing and entanglement in cavity magnonics, Phys. Rev. Research **3**, 023126 (2021).

[41] W.-J. Wu, Y.-P. Wang, J.-Z. Wu, J. Li, and J. Q. You, Remote magnon entanglement between two massive ferrimagnetic spheres via cavity optomagnonics, Phys. Rev. A **104**, 023711 (2021).

[42] R. Raussendorf and H. J. Briegel, A One-Way Quantum Computer, Phys. Rev. Lett. **86**, 5188 (2001).

[43] E. Knill, R. Laflamme, and G. J. Milburn, A scheme for efficient quantum computation with linear optics, Nature (London) **409**, 46 (2001).

[44] T. D. Ladd, F. Jelezko, R. Laflamme, Y. Nakamura, C. Monroe, and J. L. O'Brien, Quantum computers, Nature (London) **464**, 45 (2010).

[45] T. Albash and D. A. Lidar, Adiabatic quantum computation, Rev. Mod. Phys. **90**, 015002 (2018).

[46] V. Giovannetti, S. Lloyd, and L. Maccone, Quantum Metrology, Phys. Rev. Lett. **96**, 010401 (2006).

[47] V. Giovannetti, S. Lloyd, and L. Maccone, Advances in quantum metrology, Nat. Photon. **5**, 222 (2011).

[48] S. Pirandola, J. Eisert, C. Weedbrook, A. Furusawa, and S. L. Braunstein, Advances in quantum teleportation, Nat. Photon. **9**, 641 (2015).

[49] N. Lambert, C. Emary, and T. Brandes, Entanglement and the Phase Transition in Single-Mode Superradiance, Phys. Rev. Lett. **92**, 073602 (2004).

[50] V. Vedral, High-temperature macroscopic entanglement, New J. Phys. **6**, 102 (2004).

[51] W. Dür, L. Hartmann, M. Hein, M. Lewenstein, and H.-J. Briegel, Entanglement in Spin Chains and Lattices with Long-Range Ising-Type Interactions, Phys. Rev. Lett. **94**, 097203 (2005).

[52] G. Adesso and F. Illuminati, Entanglement in continuous-variable systems: Recent advances and current perspectives, J. Phys. A: Math. Theor. **40**, 7821 (2007).

[53] D. Vitali, S. Gigan, A. Ferreira, H. R. Böhm, P. Tombesi, A. Guerreiro, V. Vedral, A. Zeilinger, and M. Aspelmeyer, Optomechanical Entanglement between a Movable Mirror and a Cavity Field, Phys. Rev. Lett. **98**, 030405 (2007).

[54] C. Genes, D. Vitali, and P. Tombesi, Emergence of atom-light-mirror entanglement inside an optical cavity, Phys. Rev. A **77**, 050307(R) (2008).

[55] G. S. Agarwal and S. Huang, Strong mechanical squeezing and its detection, Phys. Rev. A **93**, 043844 (2016).

[56] A. Kamra, E. Thingstad, G. Rastelli, R.A. Duine, A. Brataas, W. Belzig, and A. Sudbo, Antiferromagnetic magnons as highly squeezed Fock states underlying quantum correlations, Phys. Rev. B **100**, 174407 (2019).

[57] R.-C. Shen, Y.-P. Wang, J. Li, S.-Y. Zhu, G. S. Agarwal, and J. Q. You, Long-Time Memory and Ternary Logic Gate using a Multistable Cavity Magnonic System, Phys. Rev. Lett. **127**, 183202 (2021).

[58] I.-C. Hoi, A. F. Kockum, T. Palomaki, T. M. Stace, B. Fan, L. Tornberg, S. R. Sathyamoorthy, G. Johansson, P. Delsing, and C. M. Wilson, Giant Cross-Kerr Effect for Propagating Microwaves Induced by an Artificial Atom, Phys. Rev. Lett. **111**, 053601 (2013).

[59] M. Kounalakis, C. Dickel, A. Bruno, N. K. Langford and G. A. Steele, Tuneable hopping and nonlinear cross-Kerr interactions in a high-coherence superconducting circuit, npj Quantum Inf. **4**, 38 (2018).

[60] A. Vrajitoarea, Z. Huang, P. Groszkowski, J. Koch, and A. A. Houck, Quantum control of an oscillator using a stimulated Josephson nonlinearity, Nat. Phys. **16**, 211 (2020).

[61] B. He, A. V. Sharypov, J. Sheng, C. Simon, and M. Xiao, Two-Photon Dynamics in Coherent Rydberg Atomic Ensemble, Phys. Rev. Lett. **112**, 133606 (2014).

[62] K. Xia, F. Nori, and M. Xiao, Cavity-Free Optical Isolators and Circulators using a Chiral Cross-Kerr Nonlinearity, Phys. Rev. Lett. **121**, 203602 (2018).

[63] J. Sinclair, D. Angulo, N. Lupu-Gladstein, K. Bonsma-Fisher, and A. M. Steinberg, Observation of a large, resonant, cross-Kerr nonlinearity in a cold Rydberg gas, Phys. Rev. Research **1**, 033193 (2019).

[64] S. Ding, G. Maslennikov, R. Hablützel, and D. Matsukevich, Cross-Kerr Nonlinearity for Phonon Counting, Phys. Rev. Lett. **119**, 193602 (2017).

[65] C. Kittel, On the theory of ferromagnetic resonance absorption, Phys. Rev. **73**, 155 (1948).

[66] W.-J. Wu, D. Xu, J. Qian, J. Li, Y.-P. Wang, and J. Q. You, Observation of magnon cross-Kerr effect in cavity magnonics, arXiv:2112.13807.

[67] P. Samuelsson, E. V. Sukhorukov, and M. Büttiker, Quasiparticle entanglement: Redefinition of the vacuum and reduced density matrix approach, New J. Phys. **7**, 176 (2005).

[68] O. A. Castro-Alvaredo, C. De Fazio, B. Doyon, and I. M. Szécsényi, Entanglement Content of Quasiparticle Excitations, Phys. Rev. Lett. **121**, 170602 (2018).

[69] J. Liu, R. Su, Y. Wei, B. Yao, S. F. Covre da Silva, Y. Yu, J. Iles-Smith, K. Srinivasan, A. Rastelli, J. Li, and X. Wang, A solid-state source of strongly entangled photon pairs with high brightness and indistinguishability, Nat. Nanotechnol. **14**, 586 (2019).

[70] A. Gloppe, R. Hisatomi, Y. Nakata, Y. Nakamura, and K. Usami, Resonant Magnetic Induction Tomography of a Magnetized Sphere, Phys. Rev. Applied **12**, 014061 (2019).

[71] D. D. Stancil and A. Prabhakar, *Spin Waves: Theory and Applications* (Springer, New York, 2009).

[72] D. F. Walls and G. J. Milburn, *Quantum Optics* (Springer, Berlin, 1994).

[73] A. G. Gurevich and G. A. Melkov, *Magnetization Oscillations and Waves* (CRC, Boca Raton, 2020).

[74] T. Holstein and H. Primakoff, Field dependence of the intrinsic domain magnetization of a ferromagnet, Phys. Rev. **58**, 1098 (1940).

[75] C. W. Gardiner and P. Zoller, *Quantum Noise*, 3rd ed. (Springer, New York, 2004).

[76] P. C. Parks and V. Hahn, *Stability Theory* (Prentice Hall, New York, 1993).

[77] G. Vidal and R. F. Werner, Computable measure of entanglement, Phys. Rev. A **65**, 032314 (2002).

[78] M. B. Plenio, Logarithmic Negativity: A Full Entanglement Monotone That is not Convex, Phys. Rev. Lett. **95**, 090503 (2005).

[79] G. Adesso and F. Illuminati, Continuous variable tangle, monogamy inequality, and entanglement sharing in Gaussian states of continuous variable systems, New J. Phys. **8**, 15 (2006).

[80] Y. Hu, G.-Q. Ge, S. Chen, X.-F. Yang, and Y.-L. Chen, Cross-Kerr-effect induced by coupled Josephson qubits in circuit quantum electrodynamics, Phys. Rev. A **84**, 012329 (2011).

[81] E. T. Holland, B. Vlastakis, R. W. Heeres, M. J. Reagor, U. Vool, Z. Leghtas, L. Frunzio, G. Kirchmair, M. H. Devoret, M. Mirrahimi, and R. J. Schoelkopf, Single-Photon-Resolved Cross-Kerr Interaction for Autonomous Stabilization of Photon-Number States, Phys. Rev. Lett. **115**, 180501 (2015).